2014

Rheological Signatures in Limit Cycle Behaviour of Dilute, Active, Polar Liquid Crystalline Polymers in Steady Shear

M. Gregory Forest

Panon Phuworawong
Old Dominion University

Qi Wang

Ruhai Zhou

Original Publication Citation

Forest, M. G., Phuworawong, P., Wang, Q., & Zhou, R. H. (2014). Rheological signatures in limit cycle behaviour of dilute, active, polar liquid crystalline polymers in steady shear. *Philosophical Transactions of the Royal Society A: Mathematical Physical and Engineering Sciences, 372*(2029), 20130362. doi:10.1098/rsta.2013.0362

PHILOSOPHICAL TRANSACTIONS OF THE ROYAL SOCIETY A

rsta.royalsocietypublishing.org

Research

Cite this article: Forest MG, Phuworawong P, Wang Q, Zhou R. 2014 Rheological signatures in limit cycle behaviour of dilute, active, polar liquid crystalline polymers in steady shear. *Phil. Trans. R. Soc. A* **372**: 20130362. http://dx.doi.org/10.1098/rsta.2013.0362

One contribution of 10 to a Theme Issue 'New trends in active liquid crystals: mechanics, dynamics and applications'.

Subject Areas:
applied mathematics, computational mathematics, mathematical modelling

Keywords:
liquid crystalline polymer, active suspension, stability analysis, numerical method, modelling

Author for correspondence:
Ruhai Zhou
e-mail: rzhou@odu.edu

Rheological signatures in limit cycle behaviour of dilute, active, polar liquid crystalline polymers in steady shear

M. Gregory Forest[1], Panon Phuworawong[2], Qi Wang[3] and Ruhai Zhou[2]

[1]Department of Mathematics, University of North Carolina at Chapel Hill, Chapel Hill, NC 27599, USA
[2]Department of Mathematics and Statistics, Old Dominion University, Norfolk, VA 23529, USA
[3]Department of Mathematics, University of South Carolina, Columbia, SC 29208, USA

We consider the dilute regime of active suspensions of liquid crystalline polymers (LCPs), addressing issues motivated by our kinetic model and simulations in Forest *et al.* (Forest *et al.* 2013 *Soft Matter* **9**, 5207–5222 (doi:10.1039/c3sm27736d)). In particular, we report *unsteady* two-dimensional heterogeneous flow-orientation attractors for pusher nanorod swimmers at *dilute* concentrations where passive LCP equilibria are isotropic. These numerical limit cycles are analogous to longwave (homogeneous) tumbling and kayaking limit cycles and two-dimensional heterogeneous unsteady attractors of passive LCPs in weak imposed shear, yet these states arise exclusively at *semi-dilute* concentrations where stable equilibria are nematic. The results in Forest *et al.* mentioned above compel two studies in the dilute regime that complement recent work of Saintillan & Shelley (Saintillan & Shelley 2013 *C. R. Physique* **14**, 497–517 (doi:10.1016/j.crhy.2013.04.001)): linearized stability analysis of the isotropic state for nanorod pushers and pullers; and an analytical–numerical study of weakly and strongly sheared active polar nanorod suspensions to capture how particle-scale activation affects shear rheology. We find that weakly sheared dilute puller versus pusher suspensions exhibit steady versus unsteady responses, shear thickening versus thinning and positive versus negative first normal stress

Royal Society Publishing

differences. These results further establish how sheared dilute nanorod pusher suspensions exhibit many of the characteristic features of sheared semi-dilute passive nanorod suspensions.

1. Introduction

In the last decade, suspensions of active (self-propelled) particles have attracted much attention and interest due to their relevance in pathology [1], ecology [2,3] and material science [4–6], yet perhaps mostly because of their remarkable coherent, self-organized behaviour on scales far removed from the individual particle species. Examples of active suspensions include swimming microorganisms, such as bacteria and microalgae, and synthetic nanoparticles that propel themselves via chemical reactions or external imposed magnetic fields. These swimming mechanisms have the common feature that each self-propelling particle exerts a propulsive force on the surrounding fluid resulting in fluid disturbances and hydrodynamic particle interactions that saturate in long-range aggregation and flow behaviour and bulk rheological properties. We refer the reader to several recent review articles [7–12] for a complete literature discussion.

In [13], we derived a kinetic model for polar active liquid crystalline polymers (ALCPs), that is, ensembles of polar, large molecular weight, rigid rod 'swimmers' in a viscous solvent. In the model, polarity and particle-activation physics are coupled to the Doi–Hess theory for passive liquid crystalline polymers (LCPs) [14–18]. It extends the polar hydrodynamic active liquid crystal model of Giomi, Marchetti and co-workers [9,11,19–23] and the active micro-rod suspension model of Saintillan & Shelley [24,25] to active large molecular weight rods at arbitrary equilibrium volume fractions. The resulting Doi–Hess–Smoluchowski equation inherits contributions due to spatial inhomogeneity and translational diffusion of the rod number density, rod polarity and self-propulsion, and the hydrodynamic equations inherit additional extra stress contributions. By suppression of LCP physics, our model recovers kinetic and mesoscopic active suspension theories of athermal, polar and apolar, micrometre-scale swimmers [7–9,20–22,24–30]. The authors' full orientation space, two-dimensional physical space, Smoluchowski–Navier–Stokes solver [31–34] is generalized to the new model and implemented to explore the coupling of rotational and translational diffusion, nanorod density gradients, polarity and self-propulsion, and flow feedback through polar and nematic stresses.

As noted in the abstract, the striking observations of unsteady heterogeneous ALCP attractors at dilute concentrations are strongly reminiscent of weakly sheared passive LCP attractors at semi-dilute concentrations. It is natural then to explore how dilute ALCPs respond in bulk imposed shear. There is a rich history of sheared passive liquid crystals and semi-dilute LCPs, and the remarkable tumbling, wagging, and kayaking limit cycles and pathological rheological properties that have been explored using dynamical systems tools [18,35,36] in the longwave, homogeneous (so-called monodomain) limit. Here we extend these analyses to sheared monodomains of dilute polar ALCPs.

2. Kinetic flow-orientation model of polar active liquid crystalline polymers from [13]

We recall the fundamental aspects of the kinetic flow-orientation model derived and studied in [13] for polar ALCPs. We denote the axis of symmetry of the nanorod particle by $\mathbf{m}$, physical space by $\mathbf{x}$ and time by t. We set t_0, h and c as the characteristic time, length and ALCP concentration scales, respectively, and define dimensionless variables as follows:

$$\tilde{\mathbf{x}} = \frac{\mathbf{x}}{h}, \quad \tilde{t} = \frac{t}{t_0}, \quad \tilde{\mathbf{v}} = \frac{t_0 \mathbf{v}}{h}, \quad \tilde{\tau} = \frac{\tau t_0^2}{\rho h^2} \quad \text{and} \quad \tilde{f} = \frac{f}{c}, \tag{2.1}$$

where ρ is the density of the active material system and τ is the extra stress tensor. Other fundamental physical coefficients in nanorod particle suspensions are: D_r and D_s, the rotational

Table 1. Glossary of model parameters.

parameter	description
a	shape parameter of the rod
c	characteristic nanorod density
N_1	strength of spatial inhomogeneity
α	strength of polarity potential
N	strength of nematic potential
De	Deborah number (normalized rotational relaxation rate)
D_s^*	normalized translational diffusion coefficient
U_0	self-propelled or swimming speed of the nanorod
G	normalized anisotropic stress coefficient
Re	solvent Reynolds number
Re_2, Re_3	Reynolds numbers associated with rod–solvent stresses
α_0	strength of polar-nematic stress

and translational diffusion coefficients of the rods; η the solvent viscosity; ζ_1 and ζ_2, two rod–solvent friction coefficients; k_B the Boltzmann constant; and T the absolute temperature. Normalization in terms of the characteristic length, time and stress scales yields the dimensionless groups arising in the model system of Forest *et al.* [13]:

$$\left.\begin{aligned} De = \frac{1}{t_0 D_r}, \quad D_s^* = \frac{D_s t_0}{h^2}, \quad Re = \frac{\rho h^2}{\eta t_0^2}, \quad Re_2 = \frac{\rho h^2}{\zeta_1 c k_B T t_0^2}, \\ Re_3 = \frac{\rho h^2}{\zeta_2 c k_B T t_0^2}, \quad G = \frac{3 c k_B T t_0^2}{\rho h^2}, \quad \tilde{U}_0 = \frac{U_0 t_0}{h}, \end{aligned}\right\} \tag{2.2}$$

where Re is the solvent Reynolds number, Re_2 and Re_3 are the Reynolds numbers associated with the viscous stresses of the particle–solvent interaction, De is the Deborah number ($1/De$ is the normalized rotational diffusion coefficient), D_s^* is the normalized translational diffusion coefficient, G is a normalized anisotropic stress coefficient and U_0 is the self-propelled or swimming speed of the nanorod. For simplicity, we drop the tilde on dimensionless variables in the following. (A glossary of model parameters is given in table 1.)

The dimensionless equation for the number density function (NDF) $f(\mathbf{m}, \mathbf{x}, t)$ is then given by the Smoluchowski equation

$$\begin{aligned} \frac{\partial f}{\partial t} + \nabla \cdot ((\mathbf{v} + U_0 \mathbf{m}) f) = D_s^* \nabla \cdot (\nabla f + f \nabla U) \\ + \frac{1}{De} \frac{\partial}{\partial \mathbf{m}} \cdot \left(\frac{\partial}{\partial \mathbf{m}} f + f \frac{\partial}{\partial \mathbf{m}} U \right) - \frac{\partial}{\partial \mathbf{m}} \cdot (\dot{\mathbf{m}} f), \end{aligned} \tag{2.3}$$

where ∇ represents the spatial gradient operator, and $\partial/\partial \mathbf{m} = (\mathbf{I} - \mathbf{mm}) \cdot \nabla_{\mathbf{m}}$ is the orientational gradient operator. In this paper, we consider thin films of nanorods so we idealize the nanorods as two-dimensional objects, following most of the literature and consistent with our numerical results [13] that show all dilute rod suspensions converge to planar orientation. The non-local intermolecular potential U is given by

$$U = N_1 f_0 - \alpha \mathbf{n} \cdot \mathbf{m} - 2N \mathbf{M} : \mathbf{mm} \tag{2.4}$$

with N_1, α and N representing the dimensionless strengths of the potentials for spatial inhomogeneity, polarity and nematic order, respectively. Using the notation

$$\langle\cdot\rangle_c = \frac{1}{c}\int_{\|\mathbf{m}\|=1} (\cdot) f(\mathbf{m},\mathbf{x},t)\,\mathrm{d}\mathbf{m}, \tag{2.5}$$

f_0, $\mathbf{n}$ and $\mathbf{M}$ are defined as

$$f_0(\mathbf{x},t) = \langle 1\rangle_c, \quad \mathbf{n}(\mathbf{x},t) = \langle \mathbf{m}\rangle_c \quad \text{and} \quad \mathbf{M}(\mathbf{x},t) = \langle \mathbf{mm}\rangle_c. \tag{2.6}$$

The Jeffery orbit $\dot{\mathbf{m}}$ for each rod in presumed local Stokes flow is

$$\dot{\mathbf{m}} = \mathbf{W}\cdot\mathbf{m} + a[\mathbf{D}\cdot\mathbf{m} - \mathbf{D}:\mathbf{mmm}], \tag{2.7}$$

where $0 \le a \le 1$ is a geometric particle parameter, $a = (r^2-1)/(r^2+1)$, r is the particle aspect ratio, and $\mathbf{D}$ and $\mathbf{W}$ are the symmetric and antisymmetric parts of the velocity gradient tensor, respectively.

To complete the model, the Smoluchowski equation is coupled with the incompressible Navier–Stokes equations (with $D/Dt = \partial/\partial t + \mathbf{v}\cdot\nabla$):

$$\frac{D\mathbf{v}}{Dt} = \nabla\cdot(-p\mathbf{I} + \tau_{\text{passive}} + \tau_{\text{active}}) - \gamma\langle\nabla\mu\rangle_c, \quad \nabla\cdot\mathbf{v} = 0, \tag{2.8}$$

where $\mu = \delta F/\delta f$ is the chemical potential of the ALCP system given by

$$F = \int\int [\ln f - 1 + U] f\,\mathrm{d}\mathbf{m}\,\mathrm{d}\mathbf{x}, \tag{2.9}$$

and $\gamma = ct_0^2/h^2\rho$ is a dimensionless stress coefficient of the model. The constitutive equations for passive nematic stress τ_{passive} and the active stress τ_{active} are given by

$$\tau_p = \tau_{\text{visc}} + \tau_{\text{visco-nematic}} + \tau_{\text{nematic}} + \tau_{\text{polar-nematic}}, \tag{2.10}$$

where

$$\begin{aligned}
\tau_{\text{visc}} &= \frac{2}{Re}\mathbf{D},\\
\tau_{\text{visco-nematic}} &= \frac{1}{Re_2}[\mathbf{D}\cdot\mathbf{M} + \mathbf{M}\cdot\mathbf{D}] + \frac{1}{Re_3}\langle\mathbf{mmmm}\rangle_c:\mathbf{D},\\
\tau_{\text{nematic}} &= aG\left[\mathbf{M} - \frac{1}{2}f_0\mathbf{I} - N\mathbf{M}^2 + N\mathbf{M}:\langle\mathbf{mmmm}\rangle_c\right],\\
\tau_{\text{polar-nematic}} &= -\frac{1}{6}\alpha G[2\mathbf{nn} - (\langle\mathbf{mmm}\rangle_c\cdot\mathbf{n} + \mathbf{n}\cdot\langle\mathbf{mmm}\rangle_c)]\\
\text{and}\qquad \tau_{\text{active}} &= G\zeta_{\text{a}}\left(\mathbf{M} - \frac{1}{2}f_0\mathbf{I}\right),
\end{aligned} \tag{2.11}$$

where ζ_{a} is the *stress activation parameter*, which controls the degree and type of stress imparted by the ensemble of swimming nanorods to the fluid. $\zeta_a < 0$, respectively >0, correspond to pushers and pullers; the passive LCP limit corresponds to $\zeta_a = 0$.

In the dilute monodomain regime, we neglect the long-range hydrodynamic interactions between particles and assume the suspension is spatially homogeneous as in [37,38], so that the Smolochowski equation (2.3) reduces to

$$\frac{\partial f}{\partial t} = \frac{1}{De}\frac{\partial}{\partial\mathbf{m}}\cdot\left(\frac{\partial}{\partial\mathbf{m}}f + f\frac{\partial}{\partial\mathbf{m}}U\right) - \frac{\partial}{\partial\mathbf{m}}\cdot(\dot{\mathbf{m}}f), \tag{2.12}$$

the characteristic concentration scale becomes $c = 1$, the zeroth moment of the NDF is $f_0 = 1$, and the potential strength (in equation (2.4)) for inhomogeneity vanishes, $N_1 = 0$. Note $\alpha = 0$ corresponding to apolar passive LCPs.

Table 2. Zero wavenumber eigenfunctions and their associated eigenvalues of the linearized differential operator.

k	eigenfunction	eigenvalue
1	$a_1 \sin(\varphi)$	$\frac{\alpha - 2}{2De}$
1	$b_1 \cos(\varphi)$	$\frac{\alpha - 2}{2De}$
2	$a_2 \sin(2\varphi)$	$\frac{2(N-2)}{De}$
2	$a_2 \cos(2\varphi)$	$\frac{2(N-2)}{De}$
≥ 3	$a_k \sin(k\varphi)$	$-\frac{k^2}{De}$
≥ 3	$b_k \cos(k\varphi)$	$-\frac{k^2}{De}$

3. Longwave stability of the dilute two-dimensional nanorod isotropic equilibrium: necessary conditions on nematic (N) and polar (α) potential strengths

For the quiescent state, the Smoluchowski equation reduces to (where φ is the polar angle of the axis $\mathbf{m}$, measured with respect to the flow axis (x) of the imposed shear introduced below)

$$\begin{aligned}\frac{\partial f}{\partial t} &= \frac{1}{De}\frac{\partial}{\partial \mathbf{m}} \cdot \left(\frac{\partial}{\partial \mathbf{m}} f + f \frac{\partial}{\partial \mathbf{m}} U\right) \\ &= \frac{1}{De}\left(\frac{\partial^2 f}{\partial \varphi^2} + \frac{\partial f}{\partial \varphi}\frac{\partial U}{\partial \varphi} + f\frac{\partial^2 U}{\partial \varphi^2}\right).\end{aligned} \tag{3.1}$$

The normalization condition $\int_0^{2\pi} f \, \mathrm{d}\varphi = 1$ gives the isotropic state

$$f = \frac{1}{2\pi}, \tag{3.2}$$

whose stability we analyse by setting $f = 1/2\pi + \epsilon f_1$ and substituting into (3.1). As a result, the linearized operator $\mathcal{L}$ at the isotropic state is given by

$$\begin{aligned}\mathcal{L}(f_1) = \frac{1}{De}\frac{\partial^2 f_1}{\partial \varphi^2} &+ \frac{4N}{(2\pi De)}\left[\sin(2\varphi)\left(\int_0^{2\pi} f_1 \sin(2\varphi)\,\mathrm{d}\varphi\right) + \cos(2\varphi)\int_0^{2\pi} f_1 \cos(2\varphi)\,\mathrm{d}\varphi\right] \\ &+ \frac{\alpha}{(2\pi De)}\left[\sin(\varphi)\left(\int_0^{2\pi} f_1 \sin(\varphi)\,\mathrm{d}\varphi\right) + \cos(\varphi)\int_0^{2\pi} f_1 \cos(\varphi)\,\mathrm{d}\varphi\right].\end{aligned} \tag{3.3}$$

Because of the orthogonality of the trigonometric function, the eigenfunctions of the operator $\mathcal{L}$ are scalar multiples of $\sin(k\varphi)$, or $\cos(k\varphi)$, where k is any positive integer. The eigenfunctions and their corresponding eigenvalues are summarized in table 2. Note that the eigenvalues are always negative for $k \geq 3$. For $k = 1$ and $k = 2$, the eigenvalues are $(\alpha - 2)/(2De)$ and $2(N-2)/(De)$, respectively. As a result, *the isotropic state is stable provided* $\alpha < 2$ *and* $N < 2$. This is consistent with the result in [39] when the polar and nematic order parameters are used to investigate the stability of isotropic, nematic and polar states.

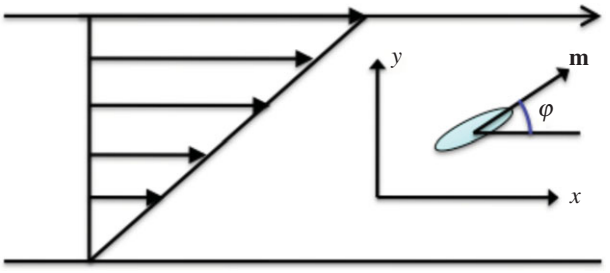

Figure 1. Steady shear flow generated by parallel plate shear cells. A nanorod axis **m** has polar angle φ measured with respect to the flow axis x. (Online version in colour.)

4. Isotropic planar two-dimensional nanorod suspensions with weak-shear perturbations: explicit asymptotic shear alignment and rheological formulae

We now perform a regular perturbation analysis to characterize the stable, weakly anisotropic equilibria of ALCPs that persist in weak shear as an extension of our earlier work on passive LCPs at dilute concentrations [40]. We consider the shear perturbed isotropic nanorod suspension confined between two parallel plates with the top plate translating at a prescribed uniform speed while the bottom plate is stationary. The velocities of intermediate layers of the fluid are assumed to increase linearly in the flow-gradient direction from the bottom to the top (figure 1). In Cartesian coordinates, the velocity is that of a simple shear

$$\mathbf{v} = \dot{\gamma} \begin{bmatrix} y \\ 0 \end{bmatrix}, \tag{4.1}$$

from which the forms of the rate-of-strain tensor $\mathbf{D}$ and the vorticity tensor W follow:

$$\mathbf{D} = \frac{1}{2}\dot{\gamma} \begin{bmatrix} 0 & 1 \\ 1 & 0 \end{bmatrix} \quad \text{and} \quad W = \frac{1}{2}\dot{\gamma} \begin{bmatrix} 0 & 1 \\ -1 & 0 \end{bmatrix}. \tag{4.2}$$

We further normalize the model equations by introducing the non-dimensionalized Peclet number $Pe = \dot{\gamma} t_0 De$ (t_0 is the characteristic time), and setting $t' = t/De$. Then the Smoluchowski equation (2.12) becomes (recall φ is measured with respect to the flow axis x in figure 1)

$$\frac{\partial f}{\partial t'} = \left(\frac{\partial^2 f}{\partial \varphi^2} + \frac{\partial f}{\partial \varphi}\frac{\partial U}{\partial \varphi} + f\frac{\partial^2 U}{\partial \varphi^2} \right) + \frac{1}{2} Pe \left(\frac{\partial f}{\partial \varphi}(1 - a\cos(2\varphi)) + 2af\sin(2\varphi) \right). \tag{4.3}$$

We first construct the distribution function, f, by positing an expansion in the Peclet number, Pe, presumed to be a small parameter $0 < Pe \ll 1$

$$f = \frac{1}{2\pi} + Pef_1 + Pe^2 f_2 + Pe^3 f_3 + \cdots \tag{4.4}$$

Substituting (4.4) into (4.3), to the first order in Pe, the steady state satisfies

$$\frac{\mathrm{d}^2 f_1}{\mathrm{d}\phi^2} + \frac{1}{2\pi}\left[\alpha \left(\cos(\varphi) \int_0^{2\pi} f_1 \cos(\varphi)\,\mathrm{d}\varphi + \sin(\varphi) \int_0^{2\pi} f_1 \sin(\varphi)\,\mathrm{d}\varphi \right) + 4N \left(\cos(2\varphi) \int_0^{2\pi} f_1 \cos(2\varphi)\,\mathrm{d}\varphi + \sin(2\varphi) \int_0^{2\pi} f_1 \sin(2\varphi)\,\mathrm{d}\varphi \right) \right] + \frac{a\sin(2\varphi)}{2\pi} = 0. \tag{4.5}$$

Using the orthogonality of the trigonometric functions, the solution for this integro-differential equation is

$$f_1 = \frac{a}{4\pi(2 - N)} \sin(2\varphi). \tag{4.6}$$

To the second order in Pe, after simplification, the steady-state equation for f_2 becomes

$$\frac{\mathrm{d}^2 f_2}{\mathrm{d}\phi^2} + \frac{1}{2\pi}\left[\alpha\left(\cos(\varphi)\int_0^{2\pi} f_2\cos(\varphi)\,\mathrm{d}\varphi + \sin(\varphi)\int_0^{2\pi} f_2\sin(\varphi)\,\mathrm{d}\varphi\right) + 4N\left(\cos(2\varphi)\int_0^{2\pi} f_2\cos(2\varphi)\,\mathrm{d}\varphi + \sin(2\varphi)\int_0^{2\pi} f_2\sin(2\varphi)\,\mathrm{d}\varphi\right)\right] - \frac{a^2\cos(4\varphi)}{2\pi(2-N)^2} + \frac{a\cos(2\varphi)}{4\pi(2-N)} = 0. \tag{4.7}$$

We again have an integro-differential equation, whose solution can be explicitly given

$$f_2 = \frac{a}{8\pi(2-N)^2}\cos(2\varphi) - \frac{a^2}{32\pi(2-N)^2}\cos(4\varphi).$$

Thus, in weak shear, the construction through second order in Pe for the number density function is

$$f \approx \frac{1}{2\pi} + Pe\left(\frac{a}{4\pi(2-N)}\sin(2\varphi)\right) + Pe^2\left(\frac{a}{8\pi(2-N)^2}\cos(2\varphi) - \frac{a^2}{32\pi(2-N)^2}\cos(4\varphi)\right). \tag{4.8}$$

Higher order approximations can be calculated in the same manner. Note that $\dot{\mathbf{m}}$ in the Smoluchowski equation contains only even Fourier modes. Therefore, in the perturbation analysis above, only even Fourier modes survive. In particular, the polarity vector $\mathbf{p}$ (the first moment of f) vanishes.

We therefore conclude that *weakly shear-perturbed two-dimensional polar ALCP suspensions from the dilute passive isotropic state are apolar and weakly nematic through* $O(Pe^2)$, with explicit shear-alignment features from the second moment of f extracted next.

From (4.8), closed-form approximations of alignment and rheological properties follow immediately. We first consider alignment properties of the shear-perturbed isotropic state. One convention to measure the orientation is to project f onto the symmetric traceless second-moment tensor $\mathbf{Q}$ given by

$$\mathbf{Q} = \langle \mathbf{mm}\rangle - \frac{\mathbf{I}}{2} = Pe\frac{a}{8(2-N)}\begin{bmatrix}0 & 1\\ 1 & 0\end{bmatrix} + Pe^2\frac{a}{16(2-N)^2}\begin{bmatrix}1 & 0\\ 0 & -1\end{bmatrix}. \tag{4.9}$$

The eigenvalues of $\mathbf{Q}$ through $O(Pe^2)$ are

$$\lambda_{1,2} = \pm\frac{aPe\sqrt{Pe^2 + 4(2-N)^2}}{16(2-N)^2}, \tag{4.10}$$

so that *the nematic order parameter* is given by

$$s = \lambda_1 - \lambda_2 = \frac{aPe\sqrt{Pe^2 + 4(2-N)^2}}{8(2-N)^2}. \tag{4.11}$$

This explicit formula reveals the weak anistropy of the sheared isotropic state and its scaling behaviour with a, *Pe and* N. The major director $\mathbf{n}_1$ (the principal axis of orientation) is a unit vector parallel to the

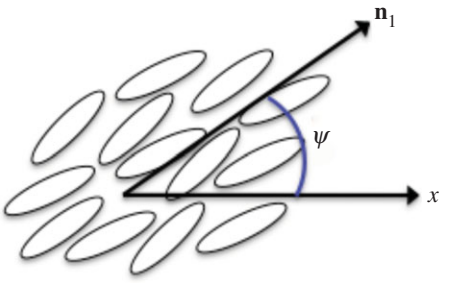

Figure 2. The major director $\mathbf{n}_1$ (the principal axis of orientation) and the alignment angle ψ for a group of nanorods. The flow direction is indicated by the x-axis. (Online version in colour.)

eigenvector associated with the largest eigenvalue λ_1:

$$\mathbf{n}_1 \sim \frac{1}{\sqrt{(Pe+\sqrt{Pe^2+4(2-N)^2})^2+(2(2-N))^2}}(Pe+\sqrt{Pe^2+4(2-N)^2},\ 2(2-N)).$$

From this, *the shear alignment angle ψ is also explicit* (figure 2):

$$\psi = \tan^{-1}\left(\frac{2(2-N)}{Pe+\sqrt{Pe^2+4(2-N)^2}}\right). \tag{4.12}$$

Note that the argument in (4.12) is smaller than 1, thus $|\psi| < 45^\circ$; *the positive angles are stable*, whereas the negative angles are unstable, by the stability criterion $2-N>0$ from above. This result implies that, being perturbed from the isotropic state by weak shear, the molecules break their random orientation and align preferentially towards the flow direction at some positive angle less than 45°. In the weak shear limit, $Pe \to 0$, the stable alignment angle is 45°.

We now derive closure approximations for the *apparent shear viscosity* σ_{xy} and the *first normal stress difference* $\mathcal{N}_1$, which are given by

$$\sigma_{xy} = \frac{\tau_{12}}{Pe}, \quad \mathcal{N}_1 = \tau_{11} - \tau_{22}, \tag{4.13}$$

where τ is the stress tensor, defined in equation (2.10). From (4.8), we note that, apart from molecular and flow parameters, only b_0, a_2 , b_2 and b_4 have non-zero values. Therefore, in weak steady shear, we arrive at the explicit formulae

$$\sigma_{xy} = \frac{aG(4\zeta_a+4-N)}{32(2-N)} + \frac{1}{2Re_2} + \frac{1}{8Re_3} + \frac{1}{Re} + \left(\frac{a^3GN}{1024(2-N)^3} + \frac{a^2}{256Re_3(2-N)^2}\right)Pe^2 \tag{4.14}$$

and

$$\mathcal{N}_1 = \frac{aG(4\zeta_a+4-N)}{32(2-N)^2}Pe^2 - \frac{a^3GN}{1024(2-N)^4}Pe^4. \tag{4.15}$$

We emphasize some immediate consequences of these formulae:

— First, note that polarity again has no influence on rheology through this order in Pe.
— Further, keeping the stability condition $N<2$ in mind, clearly ζ_a must be sufficiently negative (pusher nanorod swimmers) for $\mathcal{N}_1$ to be negative, signalling anomalous first normal stress differences that were previously implicated in tumbling and kayaking limit cycle responses of passive LCPs in imposed steady shear.

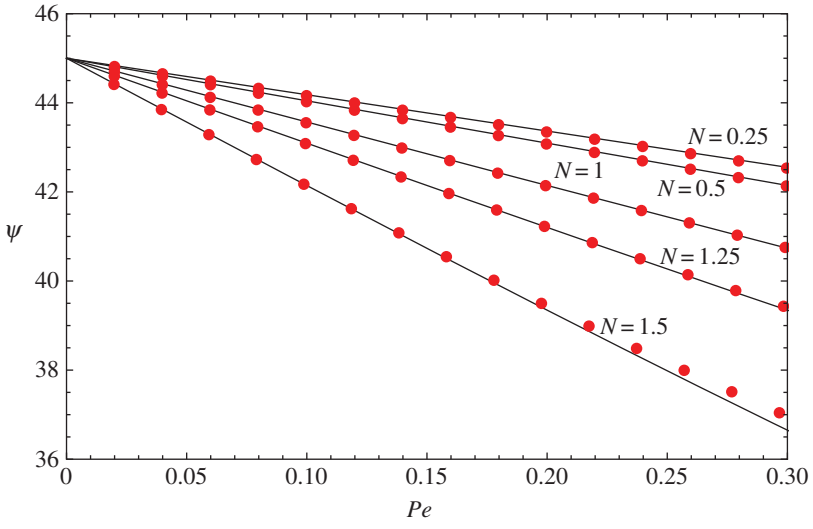

Figure 3. Comparison of scaling behaviour between our explicit asymptotic formula (4.12) (solid lines, theoretical approximation) of the alignment angle ψ and numerical results (circles). (Online version in colour.)

In the next section, we confirm these asymptotic alignment formulae and their rheological counterparts at low Pe, then show numerical results outside the asymptotic regime in §6.

5. Numerical simulations of dilute, two-dimensional polar nanorod suspensions: confirmation of the asymptotic weak shear formulae

We now confirm the asymptotic scaling formulae derived in §4 for weakly sheared steady states when $\alpha < 2$ and $N < 2$. To do so, we implement direct numerical simulations of the model (the numerical method will be described in §6). In these simulations, the polarity strength parameter is fixed at $\alpha = 1$. The aspect ratio parameter is $a = 1$ for this simulation (and for all simulations below). Then we vary the parameter nematic strength parameter N for several discrete fixed $Pe \ll 1$ and the shear rate Pe for several discrete fixed $N < 2$, showing strong agreement between the numerical simulations and the asymptotic scaling formulae. We further confirm the asymptotic predictions of the apparent shear viscosity and the first normal stress difference.

Our first observation is that, even though the polar strength parameter $\alpha \neq 0$, all odd moments in the Fourier expansion of the PDF vanish in all simulations. This confirms the asymptotic prediction: weakly sheared two-dimensional polar ALCP suspensions from the dilute isotropic state are apolar.

Figure 3 shows the nematic alignment angle versus weak shear, $0 < Pe < 0.3$, with five different dilute regime values of nematic strength, $0.25 < N < 1.5$. The solid line is the predicted angle given by (4.12), whereas the dots represent the results from numerical simulations. The asymptotics and numerics confirm that, as the shear rate increases, the nematic director tilts towards the flow direction. The weak shear asymptotic prediction is extremely accurate at low nematic strength and degrades as N approaches the critical isotropic–nematic transition value, $N = 2$.

For the order parameter s, we again plot the explicit formula (4.11) together with the numerical results in figure 4, revealing the scaling behaviour of the degree of alignment versus nematic strength $0 < N < 1.5$. The parameters chosen are $\alpha = 1$ and $Pe = 0.1$. Again, the asymptotic results are accurate at low nematic strength and weak shear, showing increased focusing of the weakly sheared orientational distribution with increasing N.

In figure 5, the apparent shear viscosity (4.13) is plotted as a function of nematic strength, $0 < N < 1.5$, for suspensions of pullers ($\zeta_a > 0$), pushers ($\zeta_a < 0$) and passive particles ($\zeta_a = 0$).

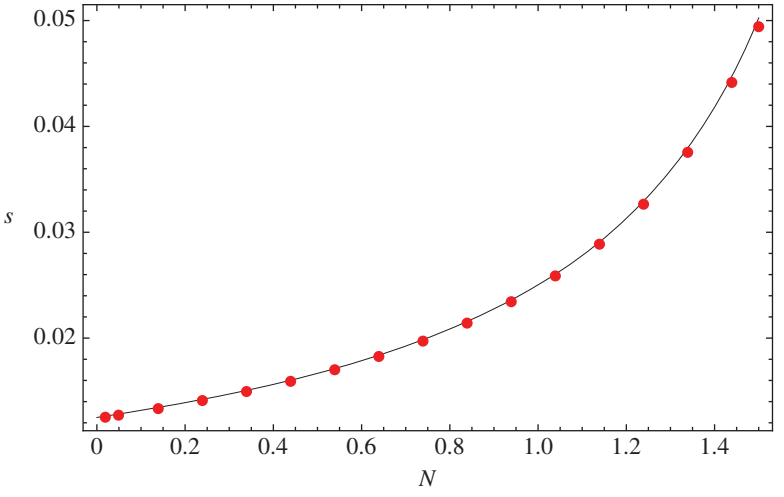

Figure 4. The comparison between the explicit asymptotic formula (4.11) (solid line, theoretical approximation) and the numerical results (circles) of the degree of orientational nanorod alignment, s (the nematic order parameter). (Online version in colour.)

Table 3. Parameter values used in figures 5 and 6 for comparison between theoretical approximations of rheological properties and numerical results.

parameter	value
a	1
Pe	0.1
G	2
c	1
α	1
N_1	1
Re	15
Re_2	15
Re_3	15
α_0	1

All parameters chosen are shown in table 3. Again, our asymptotic results are consistent with numerical results given sufficiently low nematic strength. As nematic strength increases, the apparent shear viscosity of the suspension increases (i.e. shear thickens) with puller-type particles yet decreases (shear thins) with pusher-type particles. These results simply confirm previously reported results in [37,41], and experimental results from Sokolov & Aranson [28] in which they concluded that the combined action of swimming bacteria (pushers) can reduce the viscosity of a liquid by up to a factor of seven. The experiments for puller particles are reported by Rafaï *et al.* [42] in which they observed a significant increase in viscosity as a result of the swimming activity of microalgae.

One of the anomalous signatures of passive LCPs is the observance of negative first normal stress differences in steady imposed shear. This property in shear cells translates to the confining plates being pulled towards one another. Indeed, the kinetic theory of Doi and Hess successfully predicted this behaviour, and furthermore showed that it was associated with limit cycle

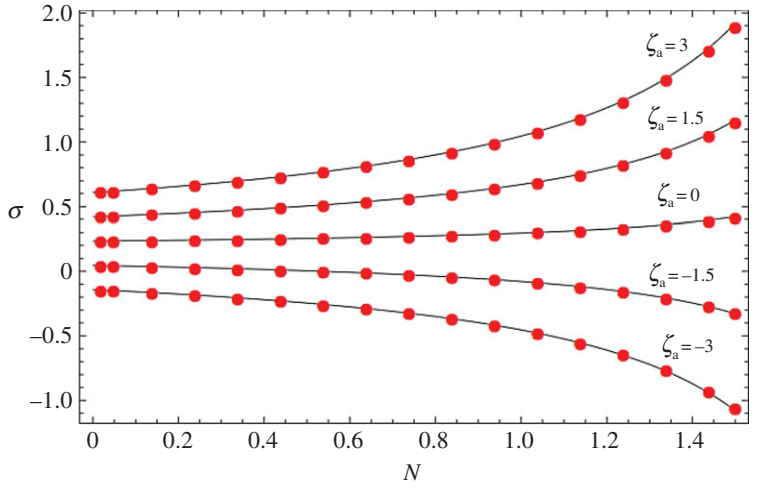

Figure 5. The comparison between theoretical approximations (solid lines) of the apparent shear viscosity, σ_{xy}, and the numerical results (circles) over a range of dilute nematic potential strengths, $0 < N < 1.5$. The stress activation parameter, ζ_a, varies from -3 to -1.5 for pushers, 0 for passive particles, and 1.5 to 3 for pullers. Other parameters are listed in table 3. (Online version in colour.)

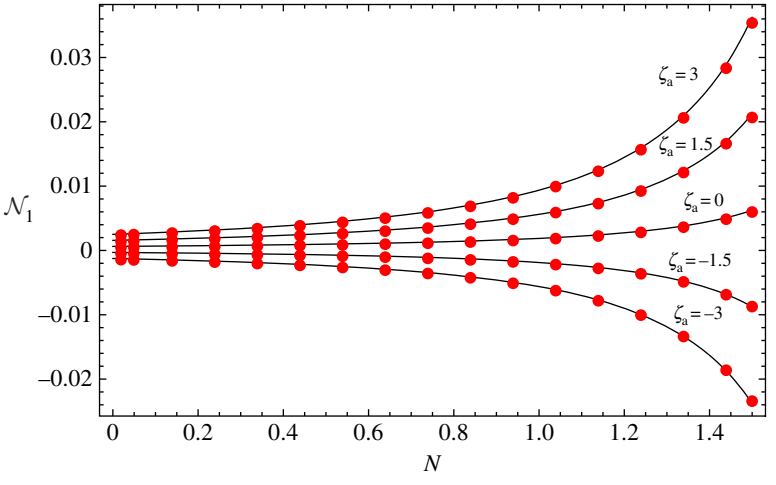

Figure 6. The comparison between theoretical approximations (solid lines) and direct numerical simulations (circles) of the normalized first normal stress difference, $\mathcal{N}_1$. The stress activation parameter, ζ_a, varies as in figure 5 from -3 to -1.5 for pushers, 0 for passive particles, and 1.5 to 3 for pullers. Other parameters are listed in table 3. (Online version in colour.)

behaviour under steady shear forcing; this was a signature achievement of the Doi–Hess theory to confirm this experimental result of sheared passive LCPs. In figure 6 (parameters shown in table 3), we find that *dilute suspensions of pusher nanorod dispersions in weak shear indeed induce negative* $\mathcal{N}_1$! Thus, the anomalous negative $\mathcal{N}_1$ behaviour of semi-dilute passive LCPs is predicted to arise at dilute concentrations for sufficiently active pusher ALCPs. In the next section, we move out of the regime of asymptotic validity and investigate the steady versus unsteady nature of the states that produce these properties. Given the history above, we anticipate that pusher ALCPs at dilute concentrations must likewise undergo an unsteady transition to limit cycle monodomain behaviour at some threshold condition to be determined.

6. Numerical kinetic simulations of dilute polar active liquid crystalline polymers at arbitrary *Pe*: shear-induced transitions to limit cycle behaviour associated with negative $\mathcal{N}_1$

Now we numerically investigate the monodomain responses of polar ALCPs in imposed steady shear of arbitrary normalized shear rate (Peclet number). The numerical method is described in the first subsection. Then we present three types of attractors: stationary steady states, tumbling limit cycles (where the major director rotates monotonically) and wagging limit cycles (where the major director oscillates without full rotations through 2π radians), and indicate the parameter variations that induce transitions between these diverse sheared, dilute, monodomain ALCP attractors. We further show how the polarity vector behaves with respect to the nematic director. Surprisingly (to us), the polarity vector always tumbles, even when the nematic director oscillates.

(a) Numerical method

For numerical simulations of planar ALCP monodomains, we approximate the number density function by a truncated Fourier series

$$f(\mathbf{m},t)\approx\frac{1}{2\pi}+\sum_{k=1}^{K}(a_k(t)\sin(k\varphi)+b_k(t)\cos(k\varphi)). \tag{6.1}$$

Substituting (6.1) into (4.3), we obtain a system of ordinary differential equations

$$\begin{aligned}
\frac{\mathrm{d}b_1}{\mathrm{d}t}&=-b_1+\frac{\pi}{2}(2N(a_2(a_1-a_3)+b_2(b_1-b_3))\\
&\quad-\alpha(a_1a_2+b_1(b_2-2b_0)))+\frac{Pe}{4}((a+2)a_1-aa_3),\\
\frac{\mathrm{d}b_2}{\mathrm{d}t}&=-4b_2-\pi((a_1(a_1+a_3)+b_1(b_3-b_1))\\
&\quad+2N(a_2a_4+b_2(b_4-2b_0)))+\frac{Pe}{2}(2a_2-aa_4),\\
\frac{\mathrm{d}b_k}{\mathrm{d}t}&=-k^2b_k-\frac{\pi k}{2}(\alpha(a_1(a_{k-1}+a_{k+1})+b_1(b_{k+1}-b_{k-1}))\\
&\quad+2N(a_2(a_{k-2}+a_{k+2})+b_2(b_{k+2}-b_{k-2})))\\
&\quad-\frac{1}{4}kPe(a(a_{k-2}+a_{k+2})-2a_k),\quad\text{where } 3\le k\le K,\\
\frac{\mathrm{d}a_1}{\mathrm{d}t}&=-a_1+\frac{\pi}{2}(\alpha(a_1(2b_0+b_2)-a_2b_1)\\
&\quad+2N(a_2(b_1+b_3)-(a_1+a_3)b_2))+\frac{Pe}{4}((a-2)b_1+ab_3),\\
\frac{\mathrm{d}a_2}{\mathrm{d}t}&=-4a_2+\pi(\alpha(a_2(2b_1+b_3)-a_3b_1)+2N(a_2(2b_0+b_4)-a_4b_2))\\
&\quad+\frac{Pe}{2}(2a(b_0+b_4)-2b_2)\\
\text{and}\quad\frac{\mathrm{d}a_k}{\mathrm{d}t}&=-k^2a_k+\frac{\pi k}{2}(\alpha(b_1(a_{k-1}-a_{k+1})+a_1(b_{k+1}+b_{k-1}))\\
&\quad+2N(b_2(a_{k-2}-a_{k+2})+a_2(b_{k-2}+b_{k+2})))\\
&\quad+\frac{1}{4}kPe(a(b_{k-2}+b_{k+2})-2b_k),\quad\text{where } 3\le k\le K.
\end{aligned} \tag{6.2}$$

(We impose $a_k=0$, $b_k=0$ for $k>K$.) In our numerical simulations, we impose $K=20$ which corresponds to a 40-dimensional dynamical system; our studies show this resolution is sufficient

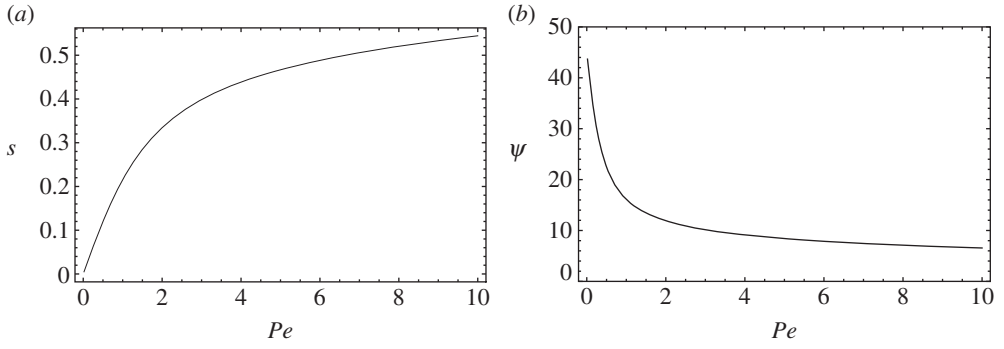

Figure 7. Stable steady-state values of (*a*) the order parameter *s* and (*b*) the alignment angle ψ versus *Pe* for $N = 1$, $\alpha = 1$.

to get converged results. Using the software AUTO [43], we produce comprehensive stable and unstable branches of steady and unsteady solutions across the multi-parameter space.

To produce rheological properties of active suspensions, the numerical data from solutions of the above system are projected onto the first and second moment tensors of the NDF. The formula for the *polarity director* $\mathbf{p}$ is easily obtained

$$\mathbf{p} = \langle \mathbf{m} \rangle = \pi \begin{bmatrix} b_1 \\ a_1 \end{bmatrix}. \tag{6.3}$$

From this, we can get the magnitude $\|\mathbf{n}\|$ (degree of polarity) and the angle ϕ of the polarity vector. The second moment tensor takes the form

$$\mathbf{Q} = \langle \mathbf{mm} \rangle - \frac{1}{2}\mathbf{I} = \frac{\pi}{2} \begin{bmatrix} b_2 & a_2 \\ a_2 & -b_2 \end{bmatrix}, \tag{6.4}$$

which yields the order parameter s and the nematic orientation angle ψ

$$s = \pi \sqrt{{a_2}^2 + {b_2}^2} \quad \text{and} \quad \psi = \tan^{-1}\left(\frac{a_2}{b_2 + \sqrt{{a_2}^2 + {b_2}^2}} \right). \tag{6.5}$$

These formulae are plotted for steady states, whereas for limit cycles we depict averages over a temporal period.

(b) Case 1: steady-state attractors for dilute, polar active liquid crystalline polymers at sufficiently low and high *Pe*

Figure 7 shows the nematic order parameter s and alignment angle ψ versus *Pe* for $N = 1$, $\alpha = 1$. Here, only one stable stationary solution branch is detected; the asymptotic results already indicate a corresponding unstable branch of steady states with negative values of ψ, which we do not plot. Increasing the flow strength (*Pe*) results in increasing *the degree of alignment. This is true for all cases below* (figure 11). As predicted previously, the alignment angle ψ tends to 45° in the limit of vanishing shear rate. The ordered state for $Pe = 4$ is shown in figure 8, where the NDF attains its maximum when $\varphi \approx 0.23$ rad $\approx 13.18°$ and $\varphi \approx 3.38$ rad $\approx 193.18°$ (head–tail symmetric).

The upshot is that for $0 < Pe$ and sufficiently weak activation parameter ζ_a, the polar ALCP distribution shear aligns in the shear plane with the nematic director in the range $45° < \psi$, where ψ converges to 0° as *Pe* increases, and the nematic order parameter s is an increasing function of *Pe*.

The values of ψ and s in the weak shear limit scale precisely as captured by the asymptotic formulae, followed by the numerical scaling in figure 6. We also find that flow-aligning always

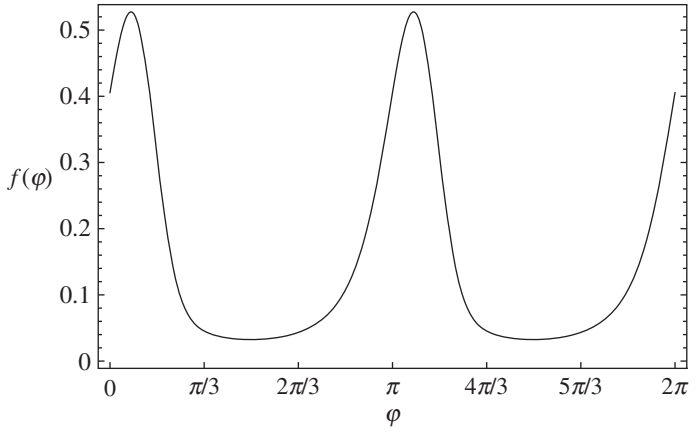

Figure 8. Stable steady state of the number density function f versus φ for $N = 1$, $\alpha = 1$, $Pe = 4$.

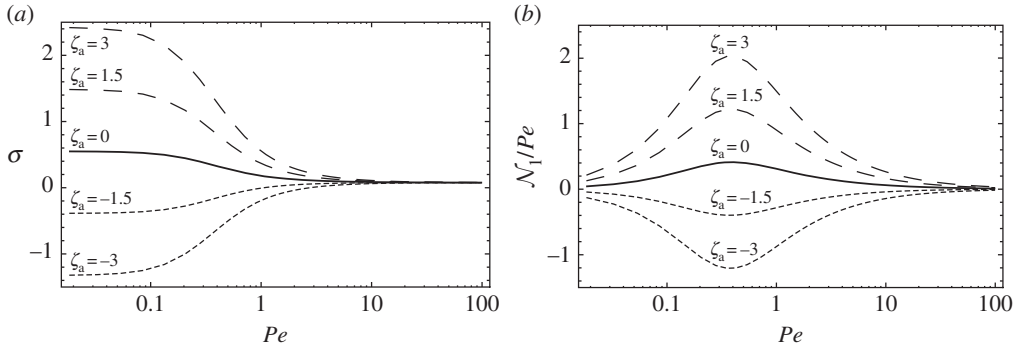

Figure 9. (*a*) Apparent shear viscosity σ_{xy} versus shear rate Pe for dilute polar ALCPs. (*b*) The first normal stress difference $\mathcal{N}_1/Pe$ versus shear rate Pe. The main parameters are $N = 1$, $\alpha = 1$. Solid line, non-stress-activated swimmers; dashed lines, puller; dotted lines, pusher.

occurs at sufficiently strong imposed shear flow (high Pe) regardless of the nematic strength, N, and the strength of polarity, α (figure 11).

The apparent shear viscosity σ for several ζ_a (stress activation) values is plotted versus Peclet number Pe in figure 9*a*. Both suspensions of pullers, $\zeta_a > 0$, and suspensions of passive particles, $\zeta_a = 0$, exhibit shear thinning behaviour, whereas suspensions of pushers, $\zeta_a < 0$, shear thicken. It can be seen that the effect of particle activation and swimming is strongest in weak flows and vanishes in strong flows (high Pe). Enhancements of σ in puller-type suspensions, and the opposite in pusher-type suspensions, in weak flows (low Pe) have been mentioned in a previous section. This phenomenon is also observed experimentally in [28,42], and obtained from the model in [37]. Figure 10*a* shows the boundary in the parameter plane (Pe–ζ_a) between positive and negative shear stress.

Figure 9*b* shows the first normal stress difference, $\mathcal{N}_1/Pe$, as a function of shear rate, Pe, for pullers, pushers and passive particles. The effect of the stress activation parameter ζ_a increases as the shear rate increases for smaller Pe and is strongest at $Pe \approx 0.5$. After that, similar to viscosity, the stress activation effect diminishes to nearly zero in strong flows. For suspensions of pullers and passive particles, $\mathcal{N}_1$ is an increasing function for $Pe < 0.5$, and then a decreasing function for $Pe > 0.5$. This behaviour is reversed for suspensions of pushers. The boundary for pusher nanorods between two regions with positive and negative first normal stress difference is shown

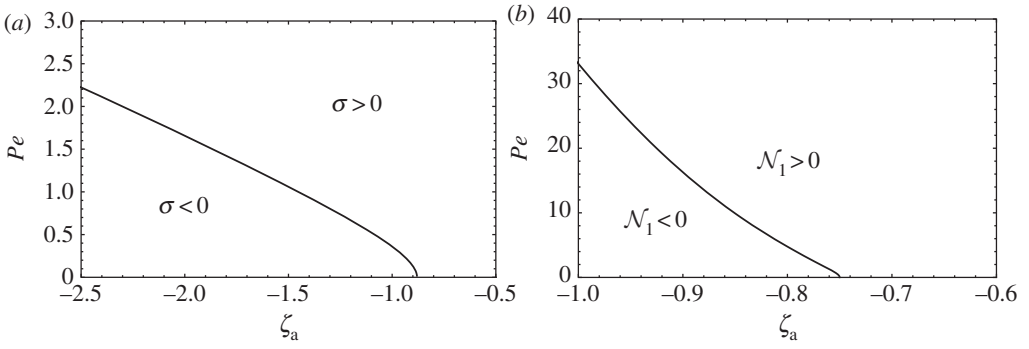

Figure 10. (*a*)Boundary in the parameter plane Pe–ζ_a that separates the regions with positive or negative stress. (*b*) Boundary in the parameter plane Pe–ζ_a that separates the regions with positive and negative first normal stress difference. Parameter values are the same as in figure 7.

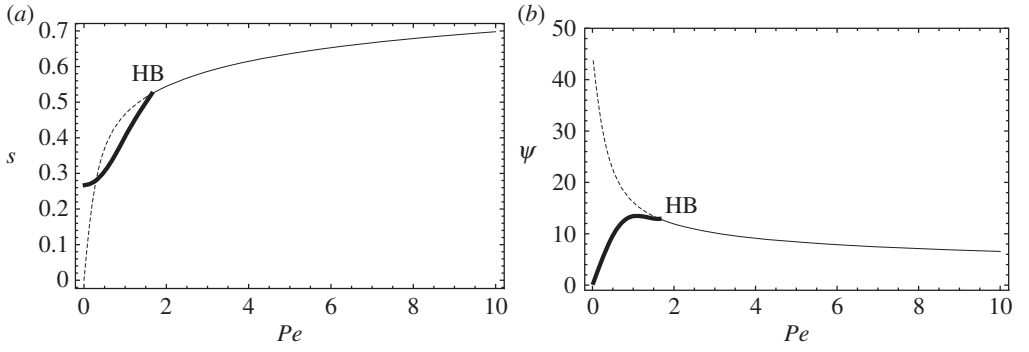

Figure 11. Bifurcation diagram of (*a*) the order parameter s and (*b*) the alignment angle ψ versus shear rate Pe for $N = 1$, $\alpha = 4$. Thick solid line, stable periodic branch; thin solid line, stable steady branch; dashed line, unstable steady branch.

in figure 10*b*. It is clear from the figure that the negative $\mathcal{N}_1$ always occurs in weak flows for $\zeta_a < -0.75$.

(c) Case 2: dilute, moderately polar liquid crystalline polymers: onset of limit cycles at critical Pe ($N = 1, \alpha = 4$)

Recall the weak shear analysis only describes steady states. We now present evidence of a Hopf bifurcation (HB) at critical Pe that reveals conditions for instability of isotropic steady states at the onset of shear, and the emergence of stable limit cycles in their place. This situation is completely analogous to the situation for stable nematic equilibria (at semi-dilute concentrations) that exhibit limit cycle responses at the onset of weak steady shear.

Figure 11 presents the bifurcation diagram for the same dilute nematic strength $N = 1$, but larger polarity strength $\alpha = 4$. The steady states at low shear, $0 < Pe < 1.84$, are now *unstable*, and *the unique stable responses are periodic limit cycles over this entire range of Pe*. The limit cycles are detected by a HB at $Pe \sim 1.84$ where the steady aligned state stabilizes for larger Pe, and the stable limit cycle branch continues back at lower Pe. The mean values of s and ψ are shown in figure 11, where it is evident that *this polar ALCP limit cycle has finite, non-zero degree of alignment for arbitrarily weak Pe*. We can see that both periodic and steady solutions arise, which are represented by thick and ordinary solid lines, respectively. Figure 12 is a phase diagram showing the boundary in the (Pe–α) parameter plane that separates the stable limit cycles and steady states.

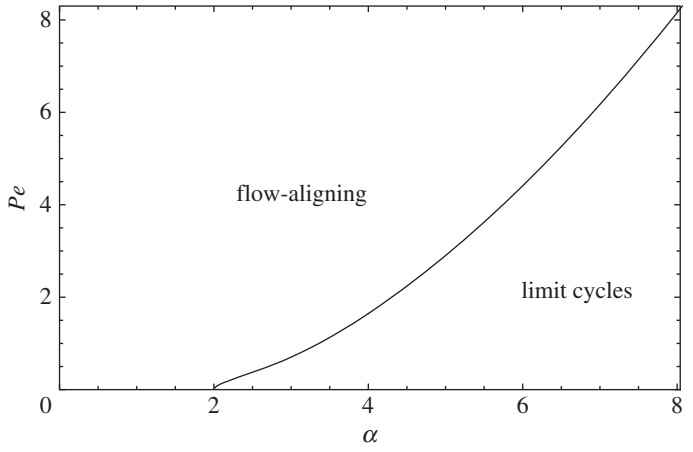

Figure 12. Critical flow strength *Pe*, below which an oscillation response occurs, as a function of polarity potential strength α for fixed $N = 1$.

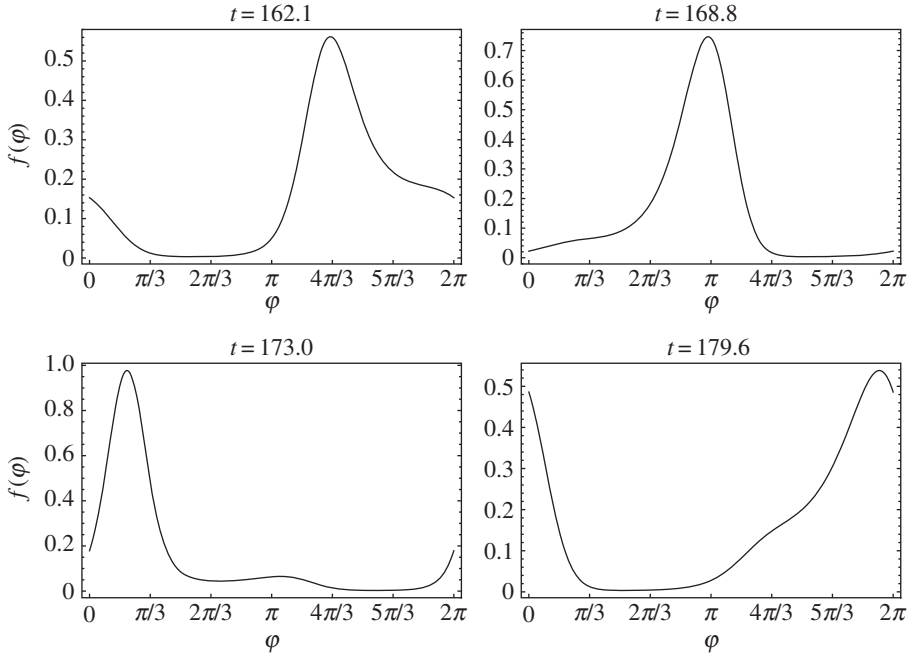

Figure 13. Four snapshots of the number density function *f* versus φ for $N = 1, \alpha = 4$, $Pe = 1$.

We now look more carefully at the oscillatory state when $\alpha = 4$ and $Pe = 1$. Several snapshots of the NDF f are shown in figure 13. The peak of the NDF moves leftwards as time evolves. This means the active particles rotate clockwise.

As shown in figure 14, the order parameter s (figure 14*a*) and the polarity magnitude $|\mathbf{p}|$ (figure 14*c*) periodically fluctuate (with period ≈ 9.6 in normalized time units; the period of the NDF is doubled, ≈ 19.2). They attain maxima and minima almost at the same time, indicating positive correlations. Figure 14*b* shows the nematic orientation angle ψ in time, which is only defined mod π, so the plot corresponds to continuous anticlockwise rotation with a mod π reset, i.e. *shear tumbling of the nematic director*. Figure 14*d* shows tumbling of the polarity vector, which is

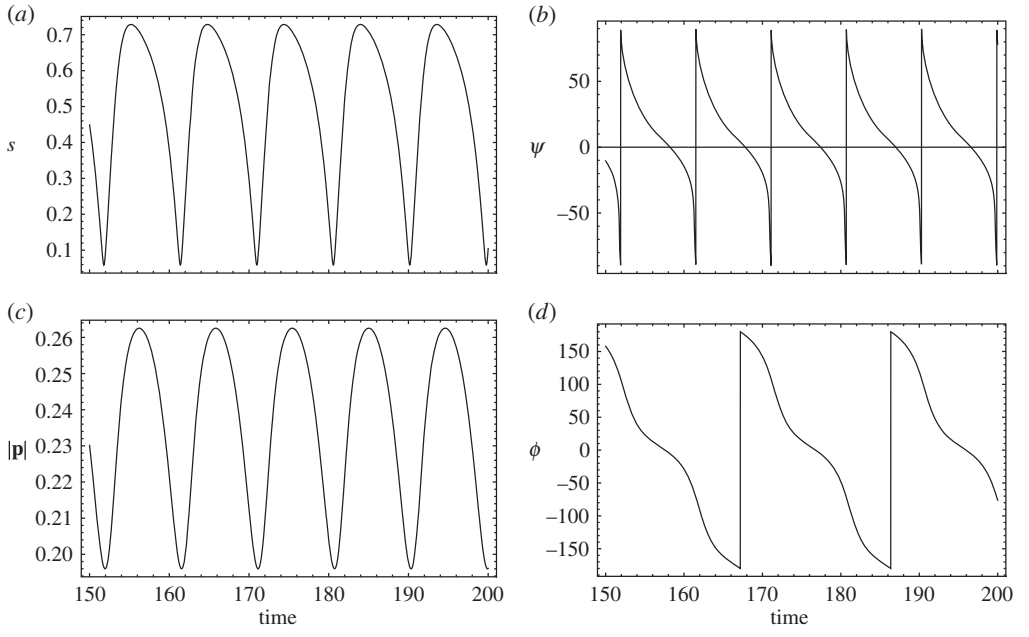

Figure 14. Time evolution of (*a*) the order parameter *s*, (*b*) the alignment angle ψ_r, (*c*) the polarity magnitude $|\mathbf{p}|$ and (*d*) the polarity angle ϕ during the tumbling state ($\alpha = 4$, $Pe = 1$). Note both the polarity and nematic director angles continuously rotate, yet are phase shifted relative to one another.

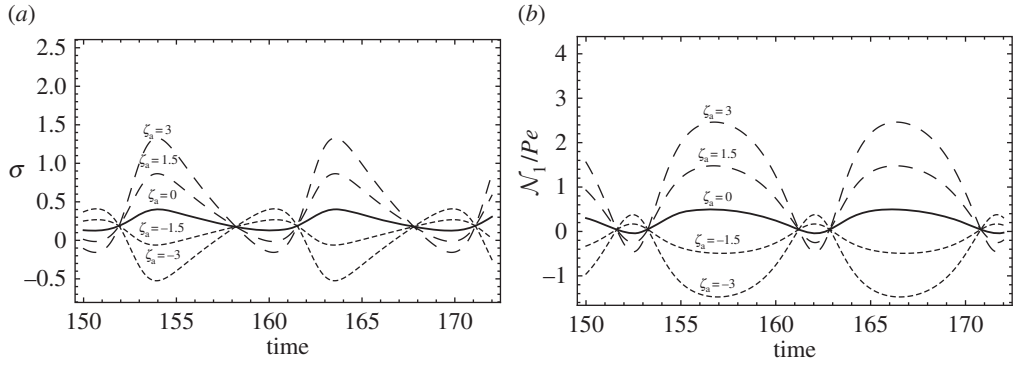

Figure 15. (*a*) Apparent shear viscosity σ_{xy} and (*b*) the normal stress difference $\mathcal{N}_1/Pe$ for the tumbling state of figure 14. Solid line, non-stress-activated swimmers; dashed lines, puller; dotted lines, pusher.

defined mod 2π, for the polarity angle as a function of time. Closer observation of the dynamics reveals the nematic and polar axes rotate slowest when they are near the flow direction and fastest when near the flow-gradient direction. The time series of effective viscosity and the first normal stress difference are plotted in figure 15 for several ζ_a values. The most striking result of figure 15 is an affirmation that *pusher limit cycles are associated with negative* $\mathcal{N}_1$ *for most of the oscillation period, with brief intervals of positive* $\mathcal{N}_1$. Puller limit cycles likewise exist, yet their time-averaged $\mathcal{N}_1$ is positive, with only brief intervals with $\mathcal{N}_1 < 0$. In all limit cycles, at least some intervals of negative $\mathcal{N}_1$ are observed!

With respect to the results for the effective viscosity, we find that pusher suspensions shear thin for most of the limit cycle and briefly shear thicken; on average, these states shear thin relative to passive polar LCPs. The opposite result obtains for pullers, which shear thicken over

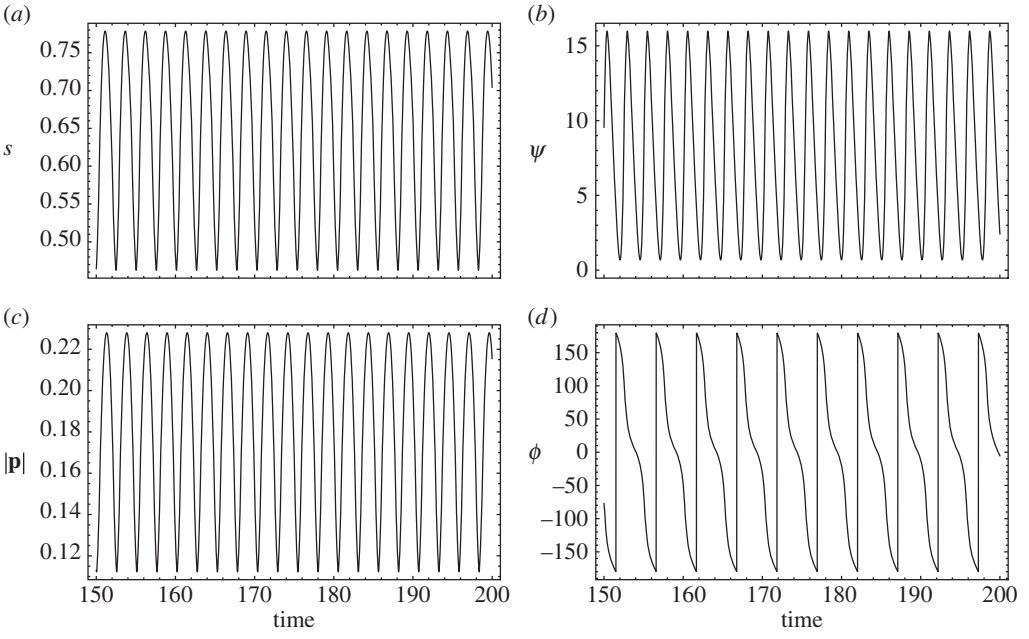

Figure 16. Time evolution of (*a*) the order parameter *s*, (*b*) the alignment angle ψ, (*c*) the polarity magnitude $|\mathbf{p}|$ and (*d*) the polarity angle ϕ during the wagging state ($\alpha = 8$, $Pe = 6$). Note the polarity angle ϕ continuously rotates while the nematic director angle ψ oscillates between 1° and 15°.

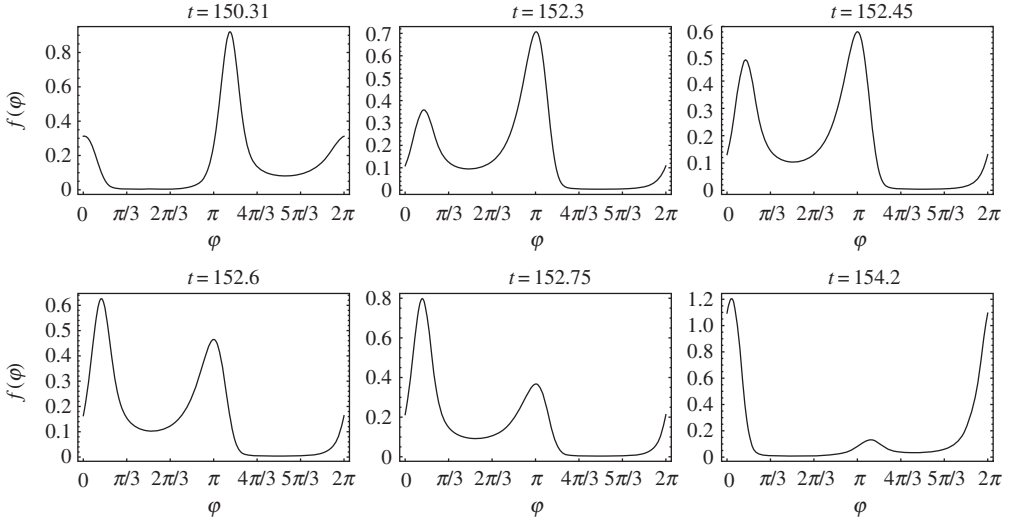

Figure 17. Snapshots of the number density function *f* versus φ for $N = 1$, $\alpha = 8$, $Pe = 6$.

most of the limit cycle period, and shear thin over a brief interval. These results are the nanorod analogue of rigorous effective viscosity analyses in [44,45], whereas similar unsteady behaviour of microscopic suspensions is shown in [46].

(d) Case 3: a hybrid polar-tumbling, nematic-wagging state

Another oscillatory state with higher frequency is shown in figures 16, 17 and 18 when $\alpha = 8$ and $Pe = 6$, still for dilute nematic strength $N = 1$. For passive liquid crystals and LCPs, this nematic

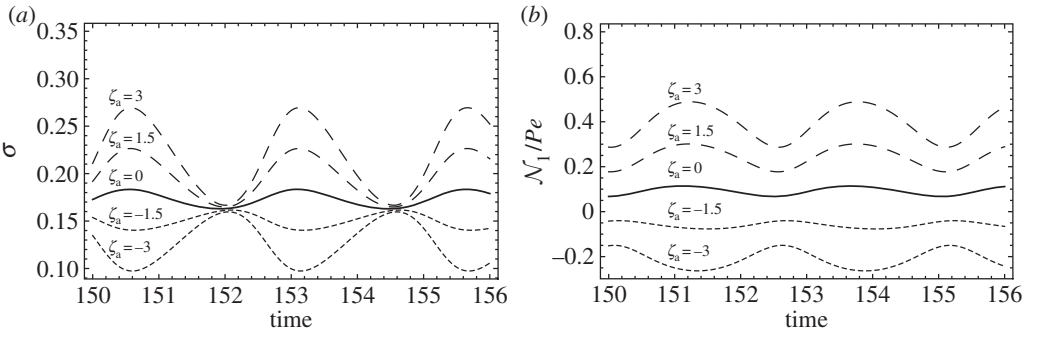

Figure 18. (*a*) Apparent shear viscosity σ_{xy} and (*b*) the first normal stress difference $\mathcal{N}_1/Pe$ in the tumbling state ($\alpha = 8$, $Pe = 6$). Solid line, non-stress-activated swimmers; dashed lines, puller; dotted lines, pusher.

director oscillation between 0.6° and 16° is called a wagging orbit. However, the corresponding time series of the polarity vector angle shows continuous clockwise rotation, or tumbling. If we look at snapshots of the NDF f in figure 17 more carefully, then there is a second maximum that is almost at the opposite direction to where the global maximum occurs. These two maxima switch roles in time (global maximum becomes second maximum, and vice versa). As shown in figure 18, the sheared active suspensions exhibit (for all times) shear thickening oscillations for pullers and shear thinning oscillations for pushers, relative to the passive polar LCP dispersion. This is distinct from figure 15 with tumbling states for both director and polarity vector, where the apparent shear viscosity fluctuates above and below that of the passive polar LCP dispersion.

7. Conclusion

This study is motivated by remarkably similar phenomena in kinetic theory modelling of two distinct nanorod dispersions: (i) two-dimensional heterogeneous unsteady attractors of active LCPs at dilute concentrations and (ii) homogeneous (monodomain) unsteady attractors of weakly sheared passive LCPs at semi-dilute concentrations. It is natural then to explore sheared, homogeneous active LCPs at dilute concentrations, the focus of this paper. We find that, indeed, particle activation physics shifts the onset of monodomain tumbling of the nanorod ensemble from the semi-dilute, nematic equilibrium regime to the dilute, isotropic equilibrium regime. Furthermore, the rheological signature of negative first normal stress differences for tumbling passive semi-dilute LCPs persists for tumbling dilute active LCPs. Additional sheared passive nematic LCP phenomena, such as the transition from director tumbling to finite oscillations (wagging) at a critical shear threshold, are shown to persist for active dilute LCPs. The polarity vector of dilute sheared active LCPs is shown to tumble for both tumbling and wagging nematic director limit cycles.

Funding statement. This research is sponsored by NSF grant nos. DMS-0908330, DMS-0908409, DMS-0908423, DMS-0943851 and DMR-1122483, the Air Force Office of Scientific Research AFOSR FA9550-12-1-0178, and the Army Research Office ARO-12-60317-MS.

References

1. Parsek MR, Singh PK. 2003 Bacterial biofilms: an emerging link to disease pathogenesis. *Annu. Rev. Microbiol.* **57**, 677–701. (doi:10.1146/annurev.micro.57.030502.090720)
2. Durham WM, Kessler JO, Stocker R. 2009 Disruption of vertical motility by shear triggers formation of thin phytoplankton layers. *Science* **323**, 1067–1070. (doi:10.1126/science.1167334)
3. Seymour JR, Marcos P, Stocker R. 2009 Resource patch formation and exploitation throughout the marine microbial food web. *Am. Nat.* **173**, E15–29. (doi:10.1086/593004)

4. Paxton WF, Kristler KC, Olmeda CC, Sen A, St Angelo SK, Cao Y, Mallouk TE, Lambert PE. 2004 Catalytic nanomotors: autonomous movement of striped nanorods. *J. Am. Chem. Soc.* **126**, 13 424–13 431. (doi:10.1021/ja047697z)
5. Paxton WF, Sen A, Mallouk TE. 2005 Motility of catalytic nanoparticles through self-generated forces. *Chem. Eur. J.* **11**, 6462–6470. (doi:10.1002/chem.200500167)
6. Stephen JE, Jonathan RH. 2010 In pursuit of propulsion at the nanoscale. *Soft Matter* **6**, 726–738. (doi:10.1039/b918598d)
7. Koch D, Subramanian G. 2011 Collective hydrodynamics of swimming micro-organisms: living fluids. *Annu. Rev. Fluid Mech.* **43**, 637–659. (doi:10.1146/annurev-fluid-121108-145434)
8. Lauga E, Powers TR, 2009 The hydrodynamics of swimming microorganisms. *Rep. Prog. Phys.* **72**, 096601. (doi:10.1088/0034-4885/72/9/096601)
9. Giomi L, Marchetti MC. 2012 Polar patterns in active fluids. *Soft Matter* **8**, 129–139. (doi:10.1039/c1sm06077e)
10. Furthauer S, Neef M, Grill SW, Kruse K, Julicher F. 2012 The Taylor–Couette motor: spontaneous flows of active polar fluids between two coaxial cylinders. *New J. Phys.* **14**, 023001. (doi:10.1088/1367-2630/14/2/023001)
11. Marchetti MC, Joanny JF, Ramaswamy S, Liverpool TB, Prost J, Rao M, Simha RA. 2013 Hydrodynamics of soft active matter. *Rev. Mod. Phys.* **85**, 1143–1189. (doi:10.1103/RevModPhys.85.1143)
12. Saintillan D. 2012 Kinetic models for biologically active suspensions. In *Natural locomotion in fluids and on surfaces: swimming, flying, and sliding* (eds S Childress, A Hosoi, WW Schultz, ZJ Wang). IMA Volumes in Mathematics and Its Applications, vol. 155, pp. 53–71. New York, NY: Springer. (doi:10.1007/978-1-4614-3997-4_4).
13. Forest MG, Wang Q, Zhou R. 2013 Kinetic theory and simulations of active polar liquid crystalline polymers. *Soft Matter* **9**, 5207–5222. (doi:10.1039/c3sm27736d)
14. Hess S. 1976 Fokker–Planck-equation approach to flow alignment in liquid crystals. *Z. Naturforsch.* **31A**, 1034–1037.
15. Kuzuu N, Doi MJ. 1983 Constitutive equation for nematic liquid crystals under weak velocity gradient derived from a molecular kinetic equation. *J. Phys. Soc. Jpn* **52**, 3486–3494. (doi:10.1143/JPSJ.52.3486)
16. Kuzuu N, Doi MJ. 1984 Constitutive equation for nematic liquid crystals under weak velocity gradient derived from a molecular kinetic equation. II. Leslie coefficients for rodlike polymers. *J. Phys. Soc. Jpn* **53**, 1031–1040. (doi:10.1143/JPSJ.53.1031)
17. Klein DH, Garcia-Cervera CJ, Ceniceros HD, Leal LG. 2005 Computational studies of the shear flow behaviour of a model for nematic liquid crystalline polymers. *ANZIAM J.* **46**, C210–C244.
18. Tsuji T, Rey AD. 1997 Effect of long range order on sheared liquid crystalline polymers. I. Compatibility between tumbling behavior and fixed anchoring. *J. Non-Newt. Fluid Mech.* **73**, 127–152. (doi:10.1016/S0377-0257(97)00037-2)
19. Baskaran A, Marchetti MC. 2008 Enhanced diffusion and ordering of self-propelled rods. *Phys. Rev. Lett.* **101**, 268101. (doi:10.1103/PhysRevLett.101.268101)
20. Baskaran A, Marchetti M. 2009 Statistical mechanics and hydrodynamics of bacterial suspensions. *Proc. Natl Acad. Sci. USA* **106**, 15 567–15 572. (doi:10.1073/pnas.0906586106)
21. Giomi L, Marchetti MC, Liverpool TB. 2008 Complex spontaneous flows and concentration banding in active polar films. *Phys. Rev. Lett.* **101**, 198101. (doi:10.1103/PhysRevLett.101.198101)
22. Giomi L, Mahadevan L, Chakraborty B, Hagan MF. 2011 Excitable patterns in active nematics. *Phys. Rev. Lett.* **106**, 218101. (doi:10.1103/PhysRevLett.106.218101)
23. Kung W, Marchetti MC, Saunders K. 2006 Hydrodynamics of polar liquid crystals. *Phys. Rev. E* **73**, 031708. (doi:10.1103/PhysRevE.73.031708)
24. Saintillan D, Shelley MJ. 2008 Instabilities and pattern formation in active particle suspensions: kinetic theory and continuum simulations. *Phys. Rev. Lett.* **100**, 178103. (doi:10.1103/PhysRevLett.100.178103)
25. Saintillan D, Shelley MJ. 2008 Instabilities, pattern formation, and mixing in active suspensions. *Phys. Fluids* **20**, 123304. (doi:10.1063/1.3041776)
26. Cates ME, Fielding SM, Marenduzzo D, Orlandini E, Yeomans JM. 2008 Shearing active gels close to the isotropic-nematic transition. *Phys. Rev. Lett.* **101**, 068102. (doi:10.1103/PhysRevLett.101.068102)

27. Ishikawa T, Locsei JT, Pedley TJ. 2008 Development of coherent structures in concentrated suspensions of swimming model micro-organisms. *J. Fluid Mech.* **615**, 401–431. (doi:10.1017/S0022112008003807)
28. Sokolov A, Aranson IS. 2009 Reduction of viscosity in suspension of swimming bacteria. *Phys. Rev. Lett.* **103**, 148101. (doi:10.1103/PhysRevLett.103.148101)
29. Sokolov A, Aranson IS, Kessler JO, Goldstein E. 2007 Concentration dependence of the collective dynamics of swimming bacteria. *Phys. Rev. Lett.* **98**, 158102. (doi:10.1103/PhysRevLett.98.158102)
30. Ryan SD, Haines BM, Berlyand L, Ziebert F, Aranson IS. 2011 Viscosity of bacterial suspensions: hydrodynamic interactions and self-induced noise. *Phys. Rev. E* **83**, 050904. (doi:10.1103/PhysRevE.83.050904)
31. Forest MG, Wang Q, Zhou R. 2004 The weak shear phase diagram for nematic polymers. *Rheol. Acta* **43**, 17–37. (doi:10.1007/s00397-003-0317-8)
32. Forest MG, Wang Q, Zhou R. 2004 The flow-phase diagram of Doi–Hess theory for sheared nematic polymers II: finite shear rates. *Rheol. Acta* **44**, 80–93. (doi:10.1007/s00397-004-0380-9)
33. Forest MG, Zhou R, Wang Q. 2005 Kinetic structure simulations of nematic polymers in plane Couette cells. II. In-plane structure transitions. *SIAM Multiscale Model. Simul.* **4**, 1280–1304. (doi:10.1137/040618187)
34. Forest MG, Zhou R, Wang Q. 2007 Nano-rod suspension flows: a 2D Smoluchowski–Navier–Stokes solver. *Int. J. Numer. Anal. Model.* **4**, 478–488.
35. Alonso EV, Wheeler AA, Sluckin TJ. 2003 Non-linear dynamics of a nematic liquid crystal in the presence of a shear flow. *Proc. R. Soc. Lond. A* **459**, 195–220. (doi:10.1098/rspa.2002.1019)
36. Chillingworth DRJ, Vicente Alonso E, Wheeler AA. 2001 Geometry and dynamics of a nematic liquid crystal in a uniform shear flow. *J. Phys. A* **34**, 1393–1404. (doi:10.1088/0305-4470/34/7/312)
37. Saintillan D. 2010 Extensional rheology of active suspensions. *Phys. Rev. E* **81**, 056307. (doi:10.1103/PhysRevE.81.056307)
38. Saintillan D. 2010 The dilute rheology of swimming suspensions: a simple kinetic model. *Exp. Mech.* **50**, 1275–1281. (doi:10.1007/s11340-009-9267-0)
39. Lee J, Forest MG, Wang Q, Zhou R. 2008 Dipole-induced, first-order phase transitions of nano-rod monolayers. *Phys. Lett. A* **372**, 3484–3487. (doi:10.1016/j.physleta.2008.01.087)
40. Forest MG, Zhou R, Wang Q. 2004 Explicit flow-aligned orientational distribution functions for dilute nematic polymers in weak shear. *J. Non-Newt. Fluid Mech.* **116**, 183–204. (doi:10.1016/j.jnnfm.2003.07.002)
41. Hatwalne Y, Ramaswamy S, Rao M, Simha RA. 2004 Rheology of active-particle suspensions. *Phys. Rev. Lett.* **92**, 118101. (doi:10.1103/PhysRevLett.92.118101)
42. Rafai S, Jibuti L, Peyla P. 2010 Effective viscosity of microswimmer suspensions. *Phys. Rev. Lett.* **104**, 098102. (doi:10.1103/PhysRevLett.104.098102)
43. Doedel EJ, Champneys AR, Fairgrive TF, Kuznetsov YA, Sandstede B, Wang X. 1996 AUTO: software for continuation and bifurcation problems in ODEs. See http://indy.cs.concordia.ca/auto.
44. Haines BM, Aranson IS, Berlyand L, Karpeev DA, 2008 Effective viscosity of dilute bacterial suspensions: a two-dimensional model. *Phys. Biol.* **5**, 046003. (doi:10.1088/1478-3975/5/4/046003)
45. Haines BM, Sokolov A, Aranson IS, Berlyand L, Karpeev DA. 2009 Three-dimensional model for the effective viscosity of bacterial suspensions. *Phys. Rev. E* **80**, 041922. (doi:10.1103/PhysRevE.80.041922)
46. Saintillan D, Shelley MJ. 2013 Active suspensions and their nonlinear models. *C. R. Physique* **14**, 497–517. (doi:10.1016/j.crhy.2013.04.001)